# Boundaries on Range-Range Constrained Admissible Regions for Optical Space Surveillance

John A. Gaebler*, Penina Axelrad†, and Paul W. Schumacher, Jr‡

**We propose a new type of admissible-region analysis for track initiation in multi-satellite problems when apparent angles measured at known stations are the only observable. The goal is to create an efficient and parallelizable algorithm for computing initial candidate orbits for a large number of new targets. It takes at least three angles-only observations to establish an orbit by traditional means. Thus one is faced with a problem that requires N-choose-3 sets of calculations to test every possible combination of the N observations. An alternative approach is to reduce the number of combinations by making hypotheses of the range to a target along the observed line-of-sight. If realistic bounds on the range are imposed, consistent with a given partition of the space of orbital elements, a pair of range possibilities can be evaluated via Lambert's method to find candidate orbits for that that partition, which then requires N-choose-2 times M-choose-2 combinations, where M is the average number of range hypotheses per observation. The contribution of this work is a set of constraints that establish bounds on the range-range hypothesis region for a given element-space partition, thereby minimizing M. Two effective constraints were identified, which together, constrain the hypothesis region in range-range space to nearly that of the true admissible region based on an orbital partition. The first constraint is based on the geometry of the vacant orbital focus. The second constraint is based on time-of-flight and Lagrange's form of Kepler's equation. A complete and efficient parallelization of the problem is possible on this approach because the element partitions can be arbitrary and can be handled independently of each other.**

## Nomenclature

| | | |
|---|---|---|
| $N$ | = | number of observations |
| $M$ | = | number of range hypotheses |
| $\rho$ | = | range hypothesis |
| $\bar{R}$ | = | observer location |
| $\bar{r}$ | = | object location |
| $e, a, p$ | = | eccentricity, semi-major axis, semi-latus rectum |
| $e_0, a_0$ | = | minimum eccentricity and semi-major axis for a given Lambert problem |
| $\Delta t_p$ | = | zero-energy orbit time-of-flight |
| $c, s$ | = | chord, semi-perimeter |
| $\alpha, \beta$ | = | angles in Lagrange time-of-flight equation |
| $\Delta t$ | = | time-of-flight between observations |
| $\Delta \nu$ | = | difference in true anomaly between observations |

## I. Motivation

One of the most difficult challenges of space surveillance is the determination of initial orbit estimates given a large set of uncorrelated observations. That is, one has no prior knowledge of the object orbits, and the observations are not explicitly associated with specific objects. Methods to identify the orbit of a newly observed object are well established. Considering optical observations, i.e. Line Of Sight (LOS) vectors, azimuth/elevation pairs, or right ascension/declination pairs, a set of three observations allows for the calculation of a preliminary orbit. This research is motivated by the combinatorial complexity of establishing preliminary orbits for a large set of new

* PhD Student, Smead Aerospace Engineering Sciences, University of Colorado
† Professor, Smead Aerospace Engineering Sciences, University of Colorado
‡ Air Force Research Laboratory, Space Surveillance Systems Branch

objects. Examples where a large number of unknown objects can appear in the surveillance volume include clustered deployments, new catalog creation, orbital collisions, and orbital break-ups. The complexity in applying classical angles-only methods stems from the need to test all possible combinations of three LOS observations from the total set of observations, an '$N$-choose-3' ($N$-3) problem, where $N$ is the number of observations under consideration. This situation can result in a prohibitively large set of combinations, as described below.

This reseach seeks methods applicable to the Geosynchronous orbital regime (GEO) where the predominate observables are optical measurements, i.e. angles and angle-rates. While some modern sensors are well-adapted to provide angle-rates, we consider angles-only here. We restrict our analysis because quality angular rates are not always available, e.g. if the orbital arc is too short or if the sampling is too sparse to allow for well conditioned, useable orbit estimates.

Also consider the potential size of the future space surveillance problem. Certainly, the lower computational complexity offered by current Constrained Admissible Region (CAR) methods is a very attractive feature if one is dealing with large space populations. However, with potentially several hundred thousand space objects being detected routinely by future optical sensor systems, it will not be feasible in practice for all optical sensors to cover their required surveillance regions in the timespans required and still be able to dwell on single targets long enough to derive accurate angle-rate estimates from sequences of discrete angles-only observations. In fact, the accuracy and precision required for the angle-rate estimates to support adequate track initiation for large populations of space objects is still an open question for current CAR range-range rate methods [1].

The advent of supercomputers motivates our desire to parallelize angles-only track initiation in large cataloging problems. Classical angles-only methods cannot be parallelized efficiently due to the $N$-3 combinations needed and the fact that the candidate orbit solutions cannot be restricted a priori to a subset of the element space. For example, if there are 1,000 new observations, there are up to 166 million combinations to test. Forming these millions of combinations is prohibitive. Our approach using element partitions and range hypotheses reduces the complexity to $N$-choose-2 ($N$-2) in the number of observations, times $M$-choose-2 ($M$-2) in the average number $M$ of range hypotheses per observation. If we use only two LOS observations then there are only 500,000 combinations to test, each with $M$-2 range hypotheses. However, this approach can be parallelized two different ways, with respect to both element partitions and pairs of range hypotheses, potentially allowing high computational throughput in the track-initiation phase of the surveillance problem.

## II. Range-Range Constrained Admissible Region

We investigated using two LOS observations to form preliminary track estimates. Since there is not enough information in two LOS observations, we assign hypotheses of the range to each LOS. The contribution of this work is a set of constraints to identify and restrict the potential values of range forming the admissible region, reducing $M$. This approach requires orbital element bounds to limit the scope of the problem. Typically sensors are designed or tuned to observe a specific region, such as optical telescopes scanning GEO, hence it is a natural extension to assume bounds on the possible orbital elements. This also works to our benefit since the problem is easily parallizeable with respect to the elements by forming partitions. Here we consider partitions on the semi-major axis and eccentricity. To develop the methodology this work focuses on a single revolution of a Keplerian GEO scenario.

While one could test every possible range value with Lambert's method to find candidate orbits, we propose to eliminate as many hypotheses as we can without generating Lambert solutions, by deriving extra geometrical and Time-Of-Flight (TOF) constraints, in order to further improve the efficiency of our approach. By this means, we believe we can make our approach feasible even for serial-computing implementations in modest-sized track-initiation problems.

There is much work in the literature on CAR methods, but typically the efforts have been focused on range-range-rate CAR that utilize angular rates. The properties and uses of the latter have been explored rather completely in recent years by Milani, Tommei, Scheeres, Maruskin, Fujimoto, DeMars, Jah and many others [2 - 9]. DeMars and Jah have shown what the admissible regions look like for partitions of semimajor axis and eccentricity by a numerical treatment of inequalities developed from the energy, angular momentum and Laplace vectors [9].

We call the set of ranges developed here the "range-range constrained admissible region" (RR-CAR) for the given angle observations and element partition. The CAR so defined is distinct from, and completely different in character from, the range-range-rate CAR defined by simultaneous angle and angle rate values. We note that the properties of the RR-CAR for pairs of line-of-sight observations and element partitions have not yet been studied systematically.

Once the RR-CAR is identified, the problem turns into a Initial Orbit Determination (IOD) of two range vectors. A Lambert solver is then used to identify the orbit of each hypothesis pair. With sufficient sampling the true orbit can be approximated by some candidate orbit, if the true orbit lies in the element partition. Each candidate orbit is a data association hypothesis that must be either confirmed or eliminated through comparisons to other observational data. Given enough range hypotheses for each observed LOS, we are guaranteed to generate a viable candidate orbit for every object that has been observed at two or more distinct times. Therefore, our approach may do a more complete job of providing candidate orbits, doing it with lower computational complexity and without any geometrical degeneracies or ill-conditioning, as compared with any traditional angles-only methods based on solving for range, including Gooding's method [10], which will always have higher computational complexity with respect to numbers of observations, require an objects to be observed at least three times, and may suffer from geometrical degeneracies or ill-conditioning.

All the traditional methods of angles-only orbit determination, plus the modern methods of Gooding, Mortari and Karimi, and others [11 - 13], rely on solving for the range by either a root-finding method or an optimization method. Such algorithms can always be made to work more reliably when rigorous upper and lower bounds on the unknown quantity are available. Nevertheless, these traditional methods will always have higher computational complexity with respect to number of observations than the method we propose here. The question of overall efficiency and throughput of our method compared to traditional methods then depends on the parallel implementation involving the element partitions, the set of observation pairs, and the set of range-hypothesis pairs within each element partition. These options for parallelization are not available with any of the above angles-only methods and offer the analyst some welcome room for creativity in his particular application.

Prior work by Roscoe and Schumacher [1] utilized three special solutions of Lambert's problem to restrict the range hypotheses. These restrictions provided lower bounds on the RR hypothesis region using the minimum eccentricity $e_0$ in Eq (9) and the minimum semimajor axis $a_0$ in Eq (8) that connect a given pair of position vectors as well as requiring a TOF longer than the zero-energy (parabolic orbit) TOF $\Delta t_p$. A range pair is rejected if $a_0 > a_{max}$, $e_0 > e_{max}$, or $t_2 - t_1 < \Delta t_p$. The RR hypothesis region was not explicitly bounded, i.e. a range pair with an infinite semi-major axis could be valid. The constraints developed in the next section provide lower and upper bounds on the range pair hypotheses given orbital element partitions.

## III. Development of Range-Range Hypothesis Constraints

Assume that we have a pair of line-of-sight unit vectors $\bar{u}_1$ and $\bar{u}_2$, measured at time $t_1$ at station position $R_1$ and time $t_2$ at station position $R_2$, respectively. Assume, without loss of generality, that $t_2 > t_1$. We want to test the hypothesis that these two observations are associated with the same space object. To this end, we attach a set of hypothetical range values, $\{\rho_{1,m}, m = 1,2, \ldots\}$ and $\{\rho_{2,n}, n = 1,2, \ldots\}$ respectively, to each of these measured unit vectors and then generate candidate orbits by solving Lambert's problem [14], [15] for each of the pair-wise combinations of hypothetical orbital position vectors $\bar{r}_{1,m}$ and $\bar{r}_{2,n}$. In the following we describe the process of restricting the hypothetical range value pairs.

Orbital element partitions are utilized to define the CAR. Thus we seek candidate orbits in a bounded region of semimajor axis $a$ and eccentricity $e$ by specifying rectangular partitions on the orbital elements as: $[a_{min}, a_{max}]$, $[e_{min}, e_{max}]$. Then building a catalog of all objects detected can be parallelized. The reason is that any partition of the space of orbital elements, including the whole space itself, can be sub-divided into smaller partitions, and each sub-partition can be handled independently. This approach allows us to consider a manageable number of range hypotheses for each sub-partition before we generate candidate orbits, simply by making the sub-partitions small enough, so that the overall computation is feasible. Moreover, by making the element partitions smaller (albeit therefore more numerous) we can reduce the number of range-hypothesis pairs that have to be considered for each observation pair for each element partition.

Roscoe et al [1] obtained some range bounds for individual observations, which can be applied a priori, as well as some conditions that permit some range pairs to be rejected without an IOD solution. A deliberately conservative first step, the range values are limited by finding the supremum range bounds based on the minimum possible perigee and maximum possible apogee for the given partition. Next range pairs are eliminated further based on the constraints developed in the subsections that follow. The remaining range hypothesis pairs are run through a Lambert solver to identify the true CAR.

If any range-pair hypothesis ($\rho_{1,2}$) does not satisfy all of the conditions described herein, then that pair of values can be eliminated from further consideration without solving Lambert's problem. Note that it is the pair of range values that is eliminated; either range value by itself may still lead to an acceptable hypothesis in combination with some other range value.

To this previous analysis we now add two constraints which efficiently bound the admissible region. As with the previous analysis [1], the efficiency of this approach derives from being able to reject range pairs without computing a Lambert solution, in fact, without iterations of any kind. Section III.A develops a constraint utilizing the geometry of the vacant focus, since orbits of interest are assumed to be elliptical (Keplerian). Section III.B develops a constraint based on the Time-Of-Flight (TOF).

### III.A. Empty Focus Constraint

Fully bounding the RR-CAR based on semi-major axis and eccentricity is possible by considering the geometry of the vacant focus. Battin [15] discusses the geometry of the vacant focus in detail. The vacant focus must lie along a hyperbola between the two position locations as shown in Figure 1. Specifying an upper limit on semi-major axis ($a_{max}$) limits how far the vacant focus can be from the positions $\{\bar{r}_1, \bar{r}_2\}$. While the eccentricity bounds ($e_{min}, e_{max}$) limit how close/far the vacant focus can lie from the primary focus, or central body.

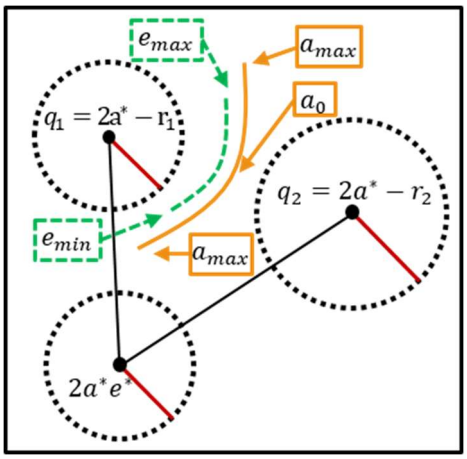


**Figure 1. Geometry of vacant focus location showing notional limits imposed by the partitions. The primary focus is the bottom circle.**

The equation of a circle around the primary focus gives a mechanism to define a constraint. The position can be developed in two dimensions $\{X, Y\}$ since it is restricted to the orbit plane and will be defined in terms of the position components and orbital parameters. Specifying limits, dictated by the partitions, on how far the vacant focus can be from origin will give a useful set of constraints. The full constraint equation is:

$$a_{min}^2 e_{min}^2 \leq \frac{a^{*2} c^2 \frac{B}{c^2}}{\|\bar{r}_1 \times \bar{r}_2\|^2} \leq a_{max}^2 e_{max}^2 \tag{1}$$

where the $(B/c^2)$ term is specified to simplify the development.

$$\frac{B}{c^2} = p^{*2} - (1 - e_0^2)(r_2 + r_1)p^* + r_1 r_2 (1 - e_0^2) \tag{2}$$

The full derivation is included in the Appendix. The semi-latus rectum $p^*$ has been introduced. For every hypothesis pair calculate the$(B/c^2)$ term with extremes of semi-latus rectum $\{p_{min}, p_{max}\}$. Then substitite into Eq (1) with similar extremes of semi-major axis $\{a_{min}, a_{max}\}$ and eccentricity $\{e_{min}, e_{max}\}$. If the position magnitudes of the hypothesis pair $\{r_1, r_2\}$ does not lie within bounds of Eq (1), reject the hypothesis pair. This description is slightly over simplified, as the function $(B/c^2)$ is parabolic, concave up, requiring some logic checking to find the true maximum and minimum values of $(B/c^2)$ to use in Eq (1).

**III.B. Time of Flight Constraint**

Typically the TOF is associated with Kepler's equation, which relates the TOF to semi-major axis, eccentricity, and the eccentric anomaly. This form is not very helpful in creating constraints. Lagrange's form of Kepler's equation proves to be much more insightful. From Prussing [16] and Battin [15]:

$$\Delta t = \sqrt{\frac{a^3}{\mu}}\left(\alpha - \beta - (\sin\alpha - \sin\beta)\right) \tag{3}$$

Where the angles $\alpha$ and $\beta$ are computed from the chord $c = \|\bar{r}_2 - \bar{r}_1\|$, the semi-perimeter $s = (r_1 + r_2 + c)/2$, and semi-major axis $a$ as follows:

$$\sin\left(\frac{\alpha}{2}\right) = \sqrt{\frac{s}{2a}} \tag{4}$$

$$\sin\left(\frac{\beta}{2}\right) = \sqrt{\frac{s - c}{2a}} \tag{5}$$

This form gives a relationship between TOF and the semi-major axis directly. Since TOF varies monotonically with $a$ for a given $\bar{r}_1$ and $\bar{r}_2$, we can bound the TOF with $\{a_{min}, a_{max}\}$. Care must be taken to handle quadrant ambiguities with the angles $\alpha$ and $\beta$. Prussing [16] provides the quadrant checks.

$$\begin{gathered}\text{if TOF} > t_0 \\ \text{then } \alpha = 2\pi - \alpha_0\end{gathered} \tag{6}$$

$$\begin{gathered}\text{if } \Delta\nu > \pi \\ \text{then } \beta = -\beta_0\end{gathered} \tag{7}$$

where the terms $\alpha_0$ and $\beta_0$ are the principal values from equations (4) and (5). In Eq (6) $t_0$ is the TOF of the miminum energy ellipse, which can be found by substituting the minimum possible semi-major axis $a_0$ for $a$ in Eq (3). The minimum value $a_0$ is a special solution to Lambert's problem as is the minimum eccentricity $e_0$:

$$a_0 = \frac{1}{4}(r_1 + r_2 + \|\bar{r}_2 - \bar{r}_1\|) \tag{8}$$

$$e_0 = |r_2 - r_1| / \|\bar{r}_2 - \bar{r}_1\| \tag{9}$$

For a given RR hypothesis, find the position vectors based on that hypothesis. Calculate $\alpha$ and $\beta$ with Eq (4) and Eq (5) using the semi-major axis partitions to obtain TOF limits. Compare the observed TOF with the partition limits to assess whether the hypothesis is valid or not.

## IV. Numerical Examples

In this section we show two examples comparing the previous efforts to the constraints proposed here.

### IV.A. Example 1

First is a simple example that illustrates what we can expect with the range bounds and range-pair criteria derived in the previous section. The satellite positions are given in Table 1. The sighting geometry is simplified by putting the station at the origin (center of the Earth), so that the observed LOS vectors lie along the radius vectors. A relatively short arc of the orbit is considered to make the problem easier to visualize. Table 2 gives the partitions of semimajor axis and eccentricity investigated. The intervals of each element happen to be centered on the given element values listed in Table 1.

**Table 1: Position data for Example 1**

| | Value |
|---|---|
| $\bar{R}$ | [0 , 0 , 0] km |
| $\bar{r}_1$ | [2624 , −10604, 5247] km |
| $\bar{r}_2$ | [6235 . −10487 , −270] km |
| $t_2 - t_1$ | 1137.8 sec |
| a | 12756 km |
| e | 0.05 |

**Table 2: Element partitions for Example 1**

| | Value |
|---|---|
| $a_{min}$ | 11756 km |
| $a_{max}$ | 13756 km |
| $e_{min}$ | 0.01 |
| $e_{max}$ | 0.09 |

Figure 2 shows the vacant focus constraint on the left and the TOF constraint on the right. The axes of the plots are the candidate $\rho_1$ and $\rho_2$, the ranges along the LOS observations in km. The axis limits are the minimum perigee and maximum apogee based on the orbital partitions in Table 2. RR hypotheses that are rejected appear in red. What is left-over is the blue region of RR hypotheses that are valid based on the constraint. The smaller region in green is the set of range pairs that define an orbit within the orbital partitions found by a Lambert solver. The true range pair is marked with the cyan asterisk.

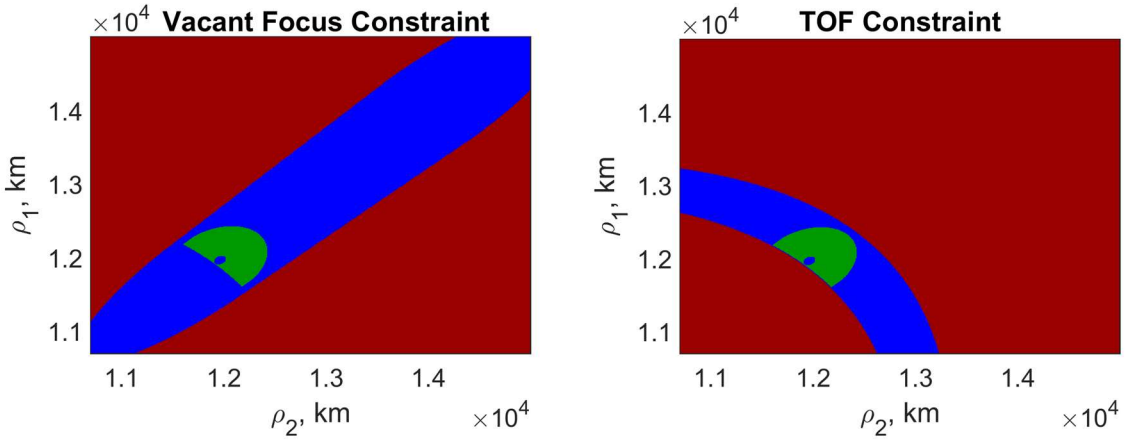


**Figure 2. Example of vacant focus constraint in left plot, and TOF constraint in right plot. Blue represents valid RR hypotheses. Red shows hypotheses that are rejected. Green is the true constrained admissible region found with Lambert's method.**

In the left plot, the region that is rejected is due to range pairs with eccentricities greater than $e_{max}$. In the right plot, the lower left region of rejected hypotheses occur because those range pairs can only have a TOF (due to the orbital partition) shorter than the given TOF. Range pairs in the upper right are rejected because they can only have a TOF that is longer the given TOF. Each range pair has an interval of possible TOF defined by $\{a_{min}, a_{max}\}$, and is rejected if the given TOF does not lie in the interval. The true CAR shown in green is representative of the complex geometries

that can exist. The 'hole' near the lower left of the region, at approximately $(\rho_1, \rho_2) = (1.2,1.2)x10^4$ km, is the set of ranges for which the eccentricity, obtained from the Lambert solver, is less than $e_{min}$.

The new constraints are compared against the Ref [1] constraints in Figure 3. The left plot shows the combination of the three special Lambert solution constraints. Rejected range hypotheses are primarily due to $e_0$ constraint violations. The right plot shows the combination of the vacant focus and TOF constraints that were shown separately in Figure 2. There is a significant reduction in the valid hypothesis region shown in blue due to the TOF constraint.

Some interesting observations can be made in comparing the various constraints. The vacant focus constraint gives similar bounds to the $e_0$ constraint proposed by Roscoe. There are some scenarios where the vacant focus constraint just overlaps the $e_0$ constraint, barely giving any benefit for the additional algebra and logic checks. However, there have been more scenarios tested where the gains are respectable relative to the simple $e_0$ checks. A few scenarios studied had slightly more hypotheses rejected by the $e_0$ constraint, but the gains were minimal. This scenario is an example where the $e_0$ constraint rejected a few more hypotheses. In the right plot of Figure 3 the blue region is slightly wider in the left and bottom corners compared to the left plot.

The TOF constraint inherently includes the $a_0$ constraint check. For small transfer angles there are significant benefits to using this TOF constraint. With larger transfer angles the benefits decrease.

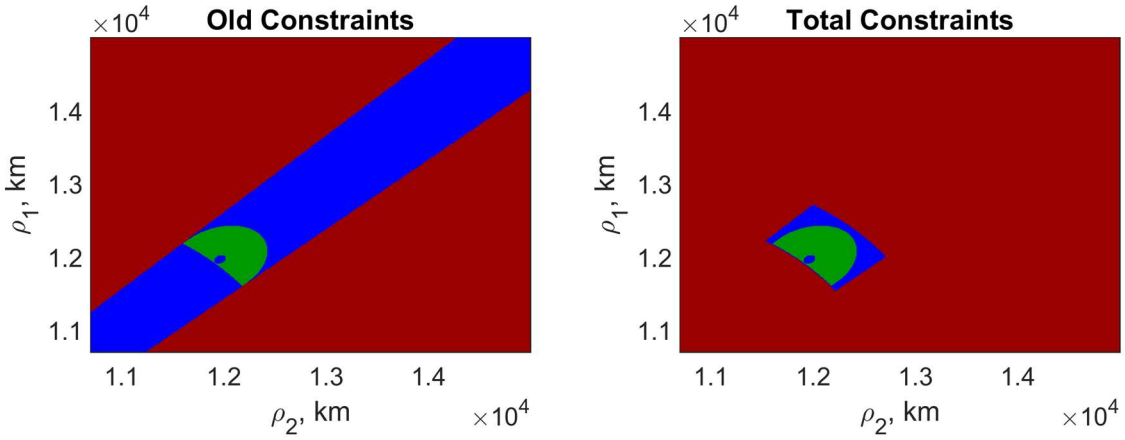


**Figure 3. Gains made with new constraints on Example 1. On left is previous best hypothesis region based on special Lambert solutions compared to the admissible region. On right is the same scenario with the new constraints implemented. Blue represents valid RR hypotheses. Red shows hypotheses that are rejected. Green is the true constrained admissible region found with Lambert's method.**

### IV.B. Example 2

The second example is more realistic, reproduced from Roscoe [1]. Table 3 provides the position data for the observer and object locations. The orbital partitions are in Table 4.

**Table 3: Positional data for second example**

| | Value |
|---|---|
| $\bar{R}_1$ | [4092 , 2690 , 4076] km |
| $\bar{R}_2$ | [3971 , 2866 , 4076] km |
| $\bar{r}_1$ | [8102 , 2576 , 5271] km |
| $\bar{r}_2$ | [5977 , 5560 , 6548] km |
| $t_2 - t_1$ | 600 sec |
| a | 11149 km |
| e | 0.145 |

**Table 4: Element partitions for second example**

| | Value |
|---|---|
| $a_{min}$ | 11049 km |
| $a_{max}$ | 11249 km |
| $e_{min}$ | 0.12 |
| $e_{max}$ | 0.1555 |

Figure 4 shows the vacant focus constraint on the left and the TOF constraint on the right. Again the axes of the plot are $\rho_1$ and $\rho_2$, the ranges along the LOS observations in km. The axis limits are the minimum perigee and maximal apogee based on the orbital partitions. The most interesting feature is the oval cut-out region of valid range hypotheses in the middle of the left plot. This feature is due to the eccentricity partition having a lower boundary, $e_{min} = 0.12$, that is greater than zero, causing the rejected hypotheses in the middle red oval. The outer oval are cases rejected due to an eccentricity greater than $e_{max}$. In this case the TOF greatly restricts the hypotheses region in the right plot. Example 2 involves a relatively small true CAR that is disconnected into two separate regions. The true range pair is marked by the cyan asterisk.

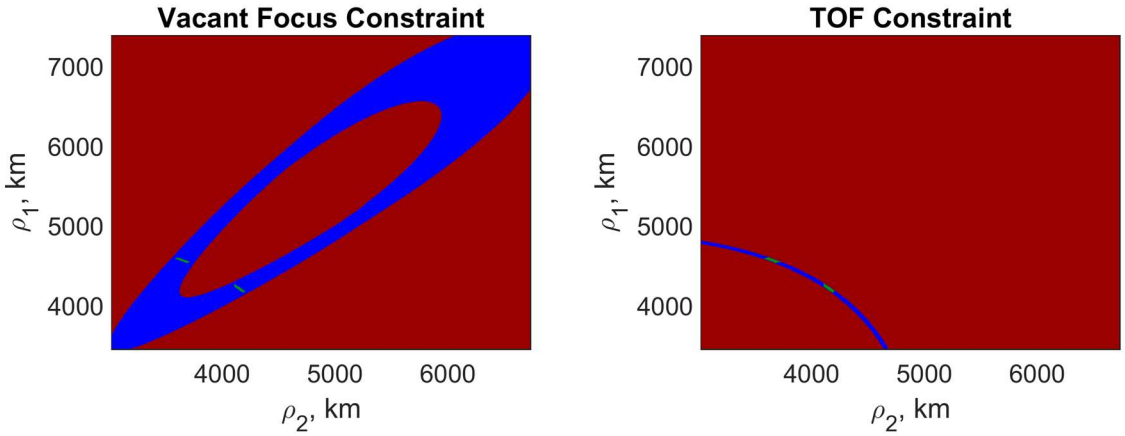


**Figure 4. Example of vacant focus constraint in left plot, and TOF constraint in right plot. Blue represents valid RR hypotheses. Red shows hypotheses that are rejected. Green is the true constrained admissible region found with Lambert's method.**

The new constraints are compared against the previous ones in **Figure 5**. The left plot shows the combination of the three special Lambert solution constraints. A similar plot can found in Roscoe [1] that also includes angle-rate bounds mapped into the RR-CAR. The upper left and lower right regions are rejected due to the $e_0$ constraint. The blue region also has a curved boundary along the upper right corner of the region where the zero-energy TOF constraint is taking effect. In the right plot is the RR-CAR using the constraints developed here.

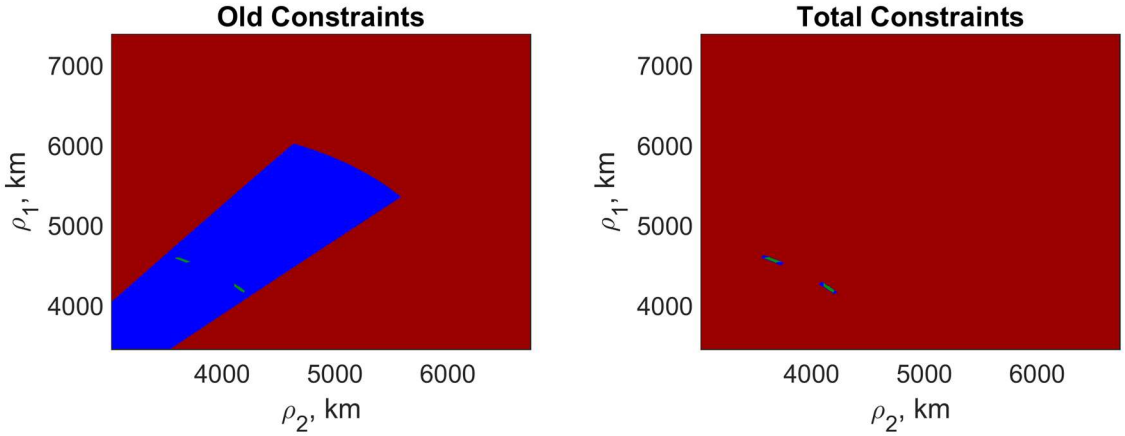


**Figure 5. Gains made with new constraints on Example 2. On left is previous best hypothesis region region based on special Lambert solutions compared to the admissible region. On right is the same scenario with the new constraints implemented. Blue represents valid RR hypotheses. Red shows hypotheses that are rejected. Green is the true constrained admissible region found with Lambert's method.**

This example shows even greater benefits from the proposed set of constraints. The CAR is very well bounded. Figure 6 shows a zoomed in view of the region of interest.

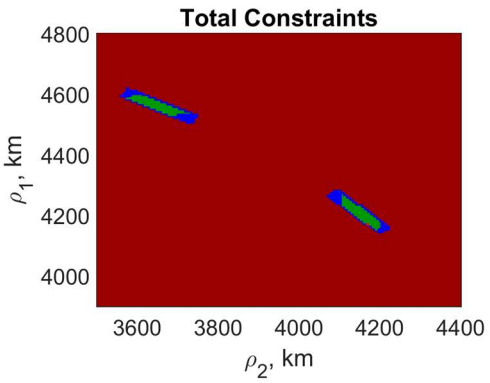


**Figure 6. Zoomed in view of the new constraints imposed. Blue represents valid RR hypotheses. Red shows hypotheses that are rejected. Green is the true constrained admissible region found with Lambert's method.**

## V. Conclusion

Constraints are proposed that can restrict range-range hypotheses used to generate candidate orbits with a Lambert solver, thereby requiring combinations of only two angles-only measurements out of the total set of observations. We are offering an efficient alternative to constructing the exact boundary of the range-range constrained admissible region *a priori*, namely, a way to test whether a pair of range hypotheses lies within the RR-CAR, which has low computational cost. These new constraints allow optimal selection of RR hypotheses such that most will lie within the true CAR. With this knowledge fewer hypotheses can be generated while still sufficiently sampling the RR-CAR. Significant gains were made in reducing the hypothesis region without rejecting true admissible cases.

There are cases identified as valid in the hypothesis region, but were not admissible. Future efforts can focus on identifying the underlying causes of this discrepancy, although it is worth noting that, in practice with a good parallel implementation, the gain in efficiency will be small and may not be worth the additional effort.

Defining partitions can be construed as dangerous in the sense that candidate orbits will be missed entirely due to poor technique in choosing the partitions. In principle, therefore, we want to be able to cover the entire space of orbital elements, in order to avoid missing any viable candidate orbits, and this may dictate the computing requirements for our method. Without covering the entire space of orbital elements, we could consider simply setting the range bounds conservatively, or overly large, in each partition. However doing so will increase the number of RR-hypothesis pairs to be tested in each partition, thereby partly negating the benefits of the method. Thinking ahead to using supercomputing resources, the problem can be parallelized by sending small partitions to different nodes, enabling us to search through a larger subset of orbital parameters in a given amount of time. Furthermore, our approach can be parallelized with respect to the angles-only observation pairs as well.

This work was restricted to single revolution cases, with transfer angles under 360°. Having run several cases, it was observed that when the transfer angle is fairly large we see a large hypothesis/admissible region. Future efforts will investigate how the constraints behave in the multi-revolution case. Also the performance benefits of the range-range hypothesis method over classic IOD methods will be assessed. The break point, where it is computationally cheaper to use the range hypotheses with a Lambert solver over classic IOD methods, will be quantified.

## Acknowledgments

The primary author gratefully acknowledges Paul Schumacher for the exposure to this work through the AFRL Scholars program. We would also like to acknowledge Chris Roscoe for his contributions and discussions toward developing the parallel track initiation method.

## References


[1] C. W. T. Roscoe, P. E. Schumacher and M. P. Wilkins, "Parallel Track Initiation for Optical Space Surveillance Using Range and Rang-Rate Bounds," in *Proceedings of the AIAA/AAS Astrodynamics Specialist Conference, AAS 13-767*, Hilton Head, SC, 2013.

[2] A. Milani, G. F. Gronchi, M. de' Michieli Vitturi and Z. Knezevic,, "Orbit Determination with Very Short Arcs. I Admissible Regions," *Celestial Mechanics and Dynamical Astronomy,* vol. 90, no. 1, pp. 57-85, 2004.

[3] A. Milani and Z. Knezevic, "From Astrometry to Celestial Mechanics: Orbit Determination with Very Short Arcs," *Celestial Mechanics and Dynamical Astronomy,* vol. 92, pp. 1-18, 2005.

[4] G. Tommei, A. Milani and A. Rossi, "Orbit Determination of Space Debris: Admissible Regions," *Celestial Mechanics and Dynamical Astronomy,* vol. 97, pp. 289-304, 2007.

[5] G. Tommei, A. Milani, D. Farnocchia and A. Rossi, "Correlation of Space Debris Observations by the Virtual Debris Algorithm," in *Proceeding of the Fifth European Conference on Space Debris*, European Space Operations Center, Darmstadt, Germany, 2009.

[6] K. Fujimoto, J. Maruskin and D. Scheeres, "Circular and Zero-Inclination Solutions for Optical Observations of Earth-Orbiting Objects," *Celestial Mechanics and Dynamical Astronomy,* vol. 106, pp. 157-182, 2010.

[7] D. Farnocchia, G. Tommei, A. Milani and A. Rossi, "Innovative Methods of Correlation and Orbit Determination for Space Debris," *Celestial Mechanics and Dynamical Astronomy,* vol. 107, pp. 169-185, 2010.

[8] G. F. Gronchi, L. Dimare and A. Milani, "Orbit Determination with the Two-Body Integrals," *Celestial Mechanics and Dynamical Astronomy,* vol. 107, pp. 299-318, 2010.

[9] K. J. DeMars and M. K. Jah, "Initial Orbit Determination via Gaussian Mixture Approximations of the Admissible Region," in *AAS Paper 12-260, Proceedings of the 22nd AAS/AIAA Space Flight Mechanics Conference*, Charleston, SC, 2012.

[10] R. H. Gooding, "A New Procedure for the Solution of the Classical Problem of Minimal Orbit Determination from Three Lines of Sight," *Celestial Mechanics and Dynamical Astronomy,* vol. 66, no. 4, pp. 387-423, 1997.

[11] R. H. Gooding, "A New Procedure for Orbit Determination Based on Three Lines of Sight (Angles Only)," Defence Research Agency, Technical Report 93004, 1993.

[12] A. J. Sarnecki, "A Projective Approach to Orbit Determination from Three Sight Lines," *Celestial Mechanics and Dynamical Astronomy,* vol. 66, no. 4, pp. 425-451, 1997.

[13] R. R. Karimi and D. Mortari, "Initial Orbit Determination Using Multiple Observations," *Celestial Mechanics and Dynamical Astronomy,* vol. 109, no. 2, pp. 167-180, 2011.

[14] R. H. Gooding, "A Procedure for the Solution of Lambert's Orbital Boundary-Value Problem," *Celestial Mechanics and Dynamical Astronomy,* vol. 48, pp. 145-165, 1990.

[15] R. H. Battin, An Introduction to the Mathematics and Methods of Astrodynamics, Reston, VA: AIAA, 1999.

[16] J. E. Prussing, "Geometrical Interpretation of the Angles alpha and beta in Lambert's Problem," *Journal of Guidance and Control,* pp. 442-443, 1979.


## Appendix: Development of Vacant Focus Constraint

First an equation for the vacant focus location $\{X, Y\}$ relative to the primary focus is needed This is accomplished by finding the common point to three circles. One is a circle around the primary focus with a radius of $2a^*e^*$. Where $a^*$ and $e^*$ are the unknown semi-major axis and eccentricity. This circle represents the farthest distance the vacant focus can be from the primary. Another circle will be around the point $P_1$ defined by $\bar{r}_1$, the hypothesized location at $t_1$. This circle will have a radius of $q_1 = 2a^* - r_1$. The last circle will be centered at $P_2$ with radius $q_2 = 2a^* - r_2$, the hypothesized location at $t_2$. See Figure 7 for a visualization of the circles defined here.

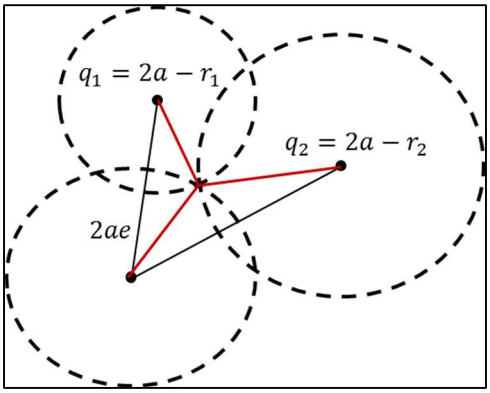


**Figure 7. Geometry used to find the location of the vacant focus relative to the primary focus (lower left point). The equations in the figure give the length of the radius for each circle (red line).**

Considering Keplerian orbits the problem is restricted to a plane, and thus can be limited to two dimensions. The system of equations for the three circles is:

$$(\mathrm{X})^2 + (\mathrm{Y})^2 = (2\mathrm{a}^*\mathrm{e}^*)^2 \tag{10}$$

$$(\mathrm{X} - \mathrm{r}_{1\mathrm{x}})^2 + \left(\mathrm{Y} - \mathrm{r}_{1\mathrm{y}}\right)^2 = (2\mathrm{a}^* - \mathrm{r}_1)^2 \tag{11}$$

$$(\mathrm{X} - \mathrm{r}_{2\mathrm{x}})^2 + \left(\mathrm{Y} - \mathrm{r}_{2\mathrm{y}}\right)^2 = (2\mathrm{a}^* - \mathrm{r}_2)^2 \tag{12}$$

In expanded form Eq (11) and Eq (12) are:

$$\mathrm{X}^2 + \mathrm{Y}^2 - 2\mathrm{r}_{1\mathrm{x}}\mathrm{X} - 2\mathrm{r}_{1\mathrm{y}}\mathrm{Y} = 4\mathrm{a}^{*2} - 4\mathrm{r}_1\mathrm{a}^* \tag{13}$$

$$\mathrm{X}^2 + \mathrm{Y}^2 - 2\mathrm{r}_{2\mathrm{x}}\mathrm{X} - 2\mathrm{r}_{2\mathrm{y}}\mathrm{Y} = 4\mathrm{a}^{*2} - 4\mathrm{r}_2\mathrm{a}^* \tag{14}$$

Substituting Eq (10) into Eq (13) and Eq (14) while also introducing the semi-latus rectum $p^*$ gives:

$$\mathrm{r}_{1\mathrm{x}}\mathrm{X} + \mathrm{r}_{1\mathrm{y}}\mathrm{Y} - 2\mathrm{r}_1\mathrm{a}^* = -2\mathrm{a}^*\mathrm{p}^* \tag{15}$$

$$\mathrm{r}_{2\mathrm{x}}\mathrm{X} + \mathrm{r}_{2\mathrm{y}}\mathrm{Y} - 2\mathrm{r}_2\mathrm{a}^* = -2\mathrm{a}^*\mathrm{p}^* \tag{16}$$

The desired location of the vacant focus $\{X, Y\}$ relative to the central body can be obtained after some algebra:

$$\mathrm{X} = \frac{2\mathrm{a}^*\mathrm{p}^*\left(\mathrm{r}_{1\mathrm{y}} - \mathrm{r}_{2\mathrm{y}}\right) + 2\mathrm{a}^*\left(+\mathrm{r}_1\mathrm{r}_{2\mathrm{y}} - \mathrm{r}_2\mathrm{r}_{1\mathrm{y}}\right)}{\mathrm{r}_1\mathrm{r}_2\sin\Delta\nu} \tag{17}$$

$$\mathrm{Y} = \frac{2\mathrm{a}^*\mathrm{p}^*(\mathrm{r}_{1\mathrm{x}} - \mathrm{r}_{2\mathrm{x}}) + 2\mathrm{a}^*(+\mathrm{r}_1\mathrm{r}_{2\mathrm{x}} - \mathrm{r}_2\mathrm{r}_{1\mathrm{x}})}{\mathrm{r}_1\mathrm{r}_2\sin\Delta\nu} \tag{18}$$

where $\Delta\nu$ is the angular separation between the two observations. Replace $X$ and $Y$ in Eq (10), perform several steps of algebra, and the equation can be reduced to:

$$\frac{4\mathrm{a}^{*2}\left(\mathrm{p}^{*2}\|\bar{r}_2 - \bar{r}_1\|^2 + 2\mathrm{p}^*\mathrm{r}_1\mathrm{r}_2(-1+\cos\Delta\nu)(\mathrm{r}_2+\mathrm{r}_1) + 2\mathrm{r}_1^2\mathrm{r}_2^2(1-\cos\Delta\nu)\right)}{\mathrm{r}_1^2\mathrm{r}_2^2\sin^2\Delta\nu} = 4\mathrm{a}^{*2}\mathrm{e}^{*2} \tag{19}$$

At this point it is convenient to specify a dummy variable $B$ as:

$$\mathrm{B} = \mathrm{p}^{*2}\|\bar{r}_2 - \bar{r}_1\|^2 + 2\mathrm{p}^*\mathrm{r}_1\mathrm{r}_2(-1+\cos\Delta\nu)(\mathrm{r}_2+\mathrm{r}_1) + 2\mathrm{r}_1^2\mathrm{r}_2^2(1-\cos\Delta\nu) \tag{20}$$

Introducing some useful identities:

$$c^2 = \|\bar{r}_2 - \bar{r}_1\|^2 \tag{21}$$

$$2r_1 r_2 \cos\Delta\nu = r_2^2 + r_1^2 - c^2 \tag{22}$$

$$e_0^2 = \frac{(r_1 - r_2)^2}{c^2} \tag{23}$$

allows Eq (20) to be presented as:

$$\frac{B}{c^2} = p^{*2} - (1 - e_0^2)(r_2 + r_1)p^* + r_1 r_2 (1 - e_0^2) \tag{24}$$

Returning to Eq (19) and introducing the orbital element partitions on semi-major axis and eccentricity, a bounded equation arises:

$$a_{min}^2 e_{min}^2 \leq \frac{a^{*2} c^2 \frac{B}{c^2}}{\|\bar{r}_1 x\, \bar{r}_2\|^2} \leq a_{max}^2 e_{max}^2 \tag{25}$$

An analysis to verify that Eq (25) is always bounded is required. Descartes rule of signs tell us that $(B/c^2)$ will always have two positive real roots, or zero real roots, and will be concave up. If there are two positive real roots, the minimum value of $(B/c^2)$ will be negative. To the left of the smaller root we will have $(B/c^2) > 0$, and decreasing wrt $p^*$. To the right of the larger root we will have $(B/c^2) > 0$, and increasing wrt $p^*$. Some logic checks are required to identify the limits to use, but the equation will always be bounded.